A stereo vision method for tracking particle flow on the weld pool surface

C. X. Zhao,[1,2,a)] I. M. Richardson,[1,2,b)] S. Kenjeres,[3,c)] C. R. Kleijn,[3,d)] and Z. Saldi[1,3,e)]
[1]*Materials Innovation Institute, Mekelweg 2, 2628 CD Delft, The Netherlands*
[2]*Department of Material Science and Engineering, Delft University of Technology, Mekelweg 2, 2628 CD Delft, The Netherlands*
[3]*Department of Multi-Scale Physics, Delft University of Technology, Prins Bernhardlaan 6, 2628 BW Delft, The Netherlands*

(Received 23 December 2008; accepted 6 May 2009; published online 17 June 2009)

The oscillation of a weld pool surface makes the fluid flow motion quite complex. Two-dimensional results cannot reflect enough information to quantitatively describe the fluid flow in the weld pool; however, there are few direct three-dimensional results available. In this paper, we describe a three-dimensional reconstruction method to measure weld pool surface features based on a single high-speed camera. A stereo adapter was added in front of the high-speed camera lens to obtain two images in the same frame from different view points at the same time. According to machine vision theory, three-dimensional parameters can be reconstructed based on two such images. In this work, three-dimensional velocity fields have been obtained using this method. Based on the calibration technique employed, the associated error is estimated to be less than 11.4%. Quantitative experimental results are useful for understanding the flow pattern, and possibly for controlling the flow of liquid in the weld pool. © *2009 American Institute of Physics*. [DOI: 10.1063/1.3143789]

I. INTRODUCTION

Measurement and sensing of weld pool features are important for the control of a welding process.[1] As a noncontact technique, vision technology is one of the most attractive methods employed to obtain quantitative results during welding. Welding involves extreme conditions, including high temperatures and strong radiation, which make contact measurements of thermal or fluid parameters in the weld pool difficult or even impossible. Most of the results reported in the literature are therefore based on numerical models to study the temperature field and velocity field in the weld pool.[2–5]

Experimental methods applied to the study of heat and mass transfer in the weld pool can be divided into the following three classes. The first is temperature measurement, where, for example, Kraus[6] observed weld pool circulation patterns by studying the weld pool surface temperature profile, and Tanaka *et al.*[7] visualized the two-dimensional (2D) temperature field of a molten pool based on Planck's law. The second is weld pool shape measurement, undertaken for example by Krasnoperov *et al.*,[8] Gao and Wu,[9] Sun *et al.*,[10] Wang *et al.*[11] and Yan *et al.*,[12] who mainly studied the pool shape after solidification and cooling. The third is fluid flow measurement, which includes qualitative assessment based on surface flow oscillation[13–16] and quantitative determination of surface flow velocity.[17–20]

Fluid flow and thermal fields are coupled together to influence the heat and mass transfer in the weld pool. Studying fluid flow is useful for understanding the final weld pool shape and energy distribution as well as the mixing of a consumable with the base material inside the weld pool. Velocity field evaluation is the main task for fluid flow measurement. In contrast to the first and the second approaches, there is a shortage of quantitative experimental results describing the complex flow motions during welding. However, quantitative measurement is always limited by prevailing conditions, such as metal vaporization, oscillation, spatter, and the small dimensions of a typical weld pool.

Most quantitative experimental work is based on surface flow measurements. Examples include Delapp *et al.*[17,18] and Henrikson,[19,20] who studied the surface flow velocity by tracing the displacement of seed particles flow using high speed video. For bulk flow observations, high energy x-rays have been used to observe tungsten particle flow and porosity formation inside a weld pool by Matsunawa and co-workers.[21,22] However, in all cases, results are based on 2D measurements, and very few particles are employed to evaluate the velocity.

In our previous work,[23] 2D particle image velocimetry (PIV) was employed to determine the weld pool surface velocity field by tracing oxide particle movement. However, the real weld pool surface is not flat but a three-dimensional (3D) curved surface induced by surface tension, and changing due to surface oscillations. Therefore, 2D PIV is limited to conditions when the surface of the weld pool is nearly flat or can be assumed to be flat. Information from the third dimension is missed in 2D measurements, which can result in significant errors under conditions where the flat surface assumption is no longer valid.

According to machine vision theory,[24] 3D reconstruction requires at least two images from different view points at the same time. Mnich *et al.*[25] measured 3D weld pool surface profiles using stereo vision. Measurements with two or more cameras can be limiting for the following reasons:

(a) Cost: High-speed cameras will increase the system cost if two or three cameras are used in welding.

[a)]Author to whom correspondence should be addressed. Electronic mail: c.zhao@tudelft.nl. Tel.: 0031-015-2786971. FAX: 0031-015-2786730.
[b)]Electronic mail: i.m.richardson@tudelft.nl. Tel.: 0031-015-2785086.
[c)]Electronic mail: s.kenjeres@tudelft.nl. Tel.: 0031-015-2783649.
[d)]Electronic mail: c.r.kleijn@tudelft.nl. Tel.: 0031-015-2782835.
[e)]Electronic mail: z.s.saldi@tudelft.nl. Tel.: 0031-015-2787084.

 © 2009 American Institute of Physics

Downloaded 15 Sep 2010 to 131.180.130.114. Redistribution subject to AIP license or copyright; see http://jap.aip.org/about/rights_and_permissions

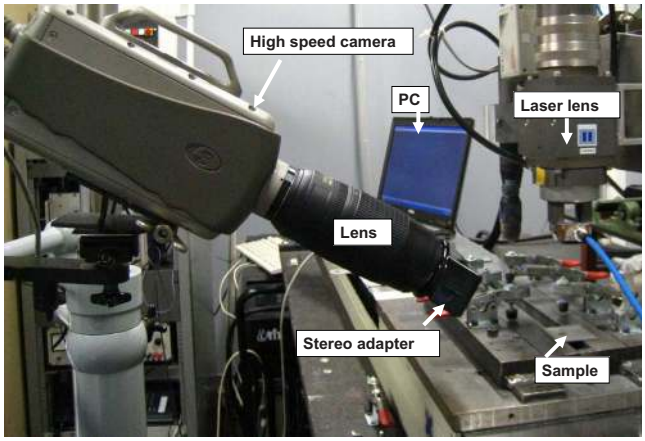

FIG. 1. (Color online) Observation system.

(b) Complexity: To remove arc illumination or strong radiation from the weld pool, two or more filters are necessary, and a synchronous device is required to control the cameras, which makes the experimental configuration more complex.
(c) Target size: The width of a normal weld pool is typically in the range 3–10 mm, which provides limited space to arrange the observation equipment.
(d) Working condition: The welding processing always generates heat and can induce both fume and spatter.

As a result, most of the reported data for 3D measurement methods are based on a single camera system (Zhao *et al.*,[26] Song and Zhang[27,28]). For example, Yoo and Lee[29] used a stereo-vision system based on a single charge-coupled device (CCD) camera and lens fitted with a biprism to acquire 3D information. However, the evaluation of 3D velocity profiles on the weld pool surface has yet to be reported. In this investigation, we address this issue using the stereo-vision approach of Yoo and Lee[29] to develop 3D flow velocity reconstructions from pairs of 2D weld pool images.

II. EXPERIMENT DESCRIPTION

A. System setup

The system arrangement is shown in Fig. 1. where the optical device consists of a complementary metal-oxide-semiconductor (CMOS) high speed camera (Phantom V5), a Pentax stereo adapter (49 mm), a Nikon 70–300 mm optical lens, some 62 mm close up lenses, and adapter rings.

A camera speed of 4000 frames/s was employed to capture sufficiently clear detail of the weld pool surface. Each frame size was 1204×256 pixels and the exposure time was 14 μs. A binary weld pool image was captured on the left and right side of each frame.

Welding was carried out using a neodymium doped yttrium aluminum garnet laser in the heat conduction mode; the maximum output power is 3000 W. The measured case considered here involves a stationary spot weld made with a beam power of 3000 W for duration of 2 s. The weld pool is open to the environment without any shielding gas, which induces inward flow motion to produce a concave weld pool surface, since oxygen influences the surface tension gradient.

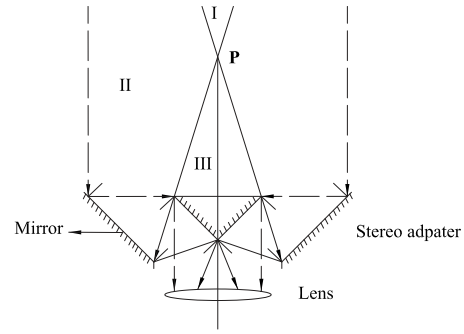

FIG. 2. Structure of the stereo adapter.

Oxide particle velocity is assumed to represent the liquid metal flow velocity on the weld pool surface. Welding was carried out on a type 304L stainless steel sample of size $2 \times 50 \times 50$ mm^3.

B. Structure of the stereo adapter

The geometric structure of the stereo adapter as shown in Fig. 2 consists of two groups of parallel mirrors arranged symmetrically with respect to the center line. Light from an object placed in front of the adapter is reflected first by the longer mirror, and then reflected again by the shorter mirror into the camera lens. Since the arranged angle of these mirrors affects the reflection direction, there are three observation zones, designated I, II, and III as shown in Fig. 2. Only one image can be captured by the camera if an object is placed in zone I, two images are available in zone II, while no image is available in zone III. The focus length should be beyond the cross point P to capture clear dual images. Both views can then be seen by a single camera, viewing the object from two slightly different angles. Thus, 3D information can be reconstructed from these two images according to machine vision theory. For a description of the optical geometry and reconstruction based on this stereo adapter, see Appendix.

III. CALIBRATION AND CORRESPONDENCE

A. Calibration

A self-calibration model was used to calibrate the left and right view using checkerboard meshes of known dimensions. Images were captured from different angles to obtain the corresponding relationship between the image Euclidean coordinate system and world Euclidean coordinate system. These boards were placed at different inclinations to the camera, to calibrate over the region required to image the weld pool. Three of calibration cases are shown in Fig. 3(a), for which the corners of diagonally adjacent black squares were selected as calibration points. A total of 117 points were employed for each calibration plate [Fig. 3(b)]. A MATLAB toolbox[30] was used to calibrate the intrinsic and extrinsic matrices of this system for both left and right views. The left top corner is considered as the origin point of the calibration plate. The origin point and three coordinate axis of world coordinate system are chosen as shown in Fig. 3(b).

Downloaded 15 Sep 2010 to 131.180.130.114. Redistribution subject to AIP license or copyright; see http://jap.aip.org/about/rights_and_permissions

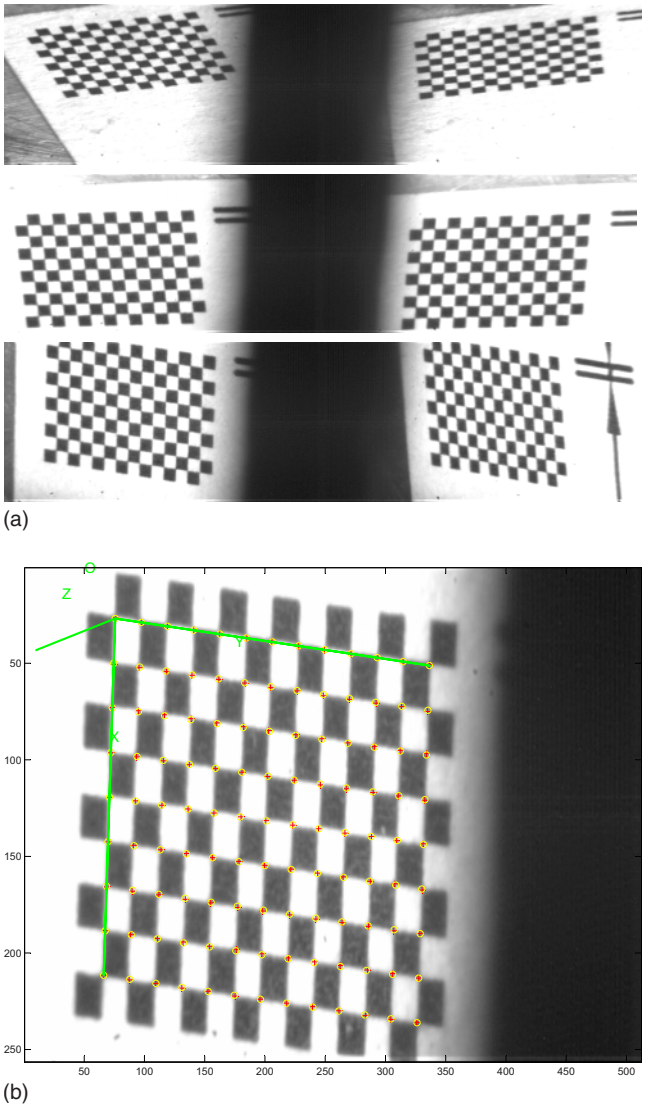

FIG. 3. (Color online) Calibration case, (a) Three of the calibration images. (b) The world Euclidean coordinate system.

In this paper, to simplify the reconstruction process, the distortion is not considered, since no obvious skew is found in the current calibration.

B. Match and correspondence

The correspondence between left and right images is evaluated by using a correlation coefficient[31] shown in Eq. (1),

$$\text{Coeff} = \frac{\sigma_{LR}^2}{\sqrt{\sigma_L^2 + \sigma_R^2}}. \tag{1}$$

The gray variances of the left and right views are given by

$$\sigma_K^2 = \sum_{i=1}^{n} \sum_{j=1}^{m} [I_K(i,j) - \mu_k]^2/(N_m \times N_m), \tag{2}$$

where K is either L or R and

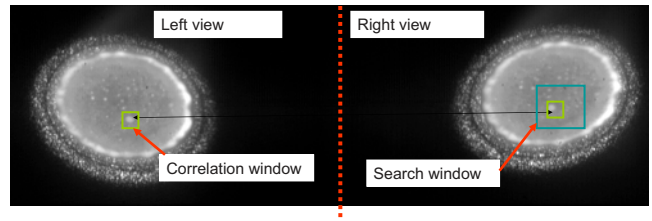

FIG. 4. (Color online) Points matching.

$$\sigma_{LR}^2 = \sum_{i=1}^{m} \sum_{j=1}^{n} \{[I_L(i,j) - \mu_L][I_R(i,j) - \mu_R]\}/(N_m \times N_m) \tag{3}$$

is the covariance between $I_L(i,j)$ and $I_R(i,j)$. $I_K(i,j)$ is the intensity value at point (i,j) and μ_K is the average value in the correlation window.

For any point P_L in the left image, a match window around this point was chosen of size $(2N_m+1)\times(2N_m+1)$ pixels, and then a larger area of size $(2N_s+1)\times(2N_s+1)$ pixels was selected as the search window, as shown in Fig. 4. Point P_R was chosen as the corresponding point when it had the highest correlation coefficient in the search window correlating with P_L. The size of the search window should be large enough to cover the potential matching point.

IV. RESULTS AND DISCUSSIONS

A. Calibration error analysis

In order to evaluate the precision of the current system, additional images are captured from another five different angles (groups 1 to 5), to compare the real dimensions with reconstructed 3D lengths using the above method. Among these five groups, the group 1 was placed horizontally, which is the same as the real welding condition. Group 4 was placed almost perpendicular to the camera lens. Other 3 groups were placed at random angles, the induced angles to camera lens are less than 45°. The width of each mesh square is 0.656 ± 0.014 mm.

Figure 5(a) shows the pixel coordinates in the image coordinate system and Fig. 5(b) the reconstructed 3D coordinates in the world coordinate system. The reconstructed 3D width of each meshes are shown in Fig. 5(c). The average measured widths for the five groups are 0.581, 0.815, 0.776, 0.683, and 0.560 mm. For each group, eight values in the x-direction along 13 square boundaries in the y-direction are reconstructed to compare with the measured width. In total, 104 values are reconstructed as shown in Fig. 5(c). The precision is different for each test case; group 4 has highest precision. From the 2D image in Fig. 5(b), group 4 shows a nearly perpendicular to the lens; the precision is reduced when the induced angle to the camera lens is decreased since many points extend outside of the focus depth. For the current weld pool flow velocity reconstruction, the welding sample was placed as the same as group 1, which was placed horizontally and inclined to the camera at an angle of 45°, its absolute error (difference between real length and reconstructed value) is 0.075 mm, representing a reconstruction relative error of 11.4% (absolute error/real length) on the sample surface.

Downloaded 15 Sep 2010 to 131.180.130.114. Redistribution subject to AIP license or copyright; see http://jap.aip.org/about/rights_and_permissions

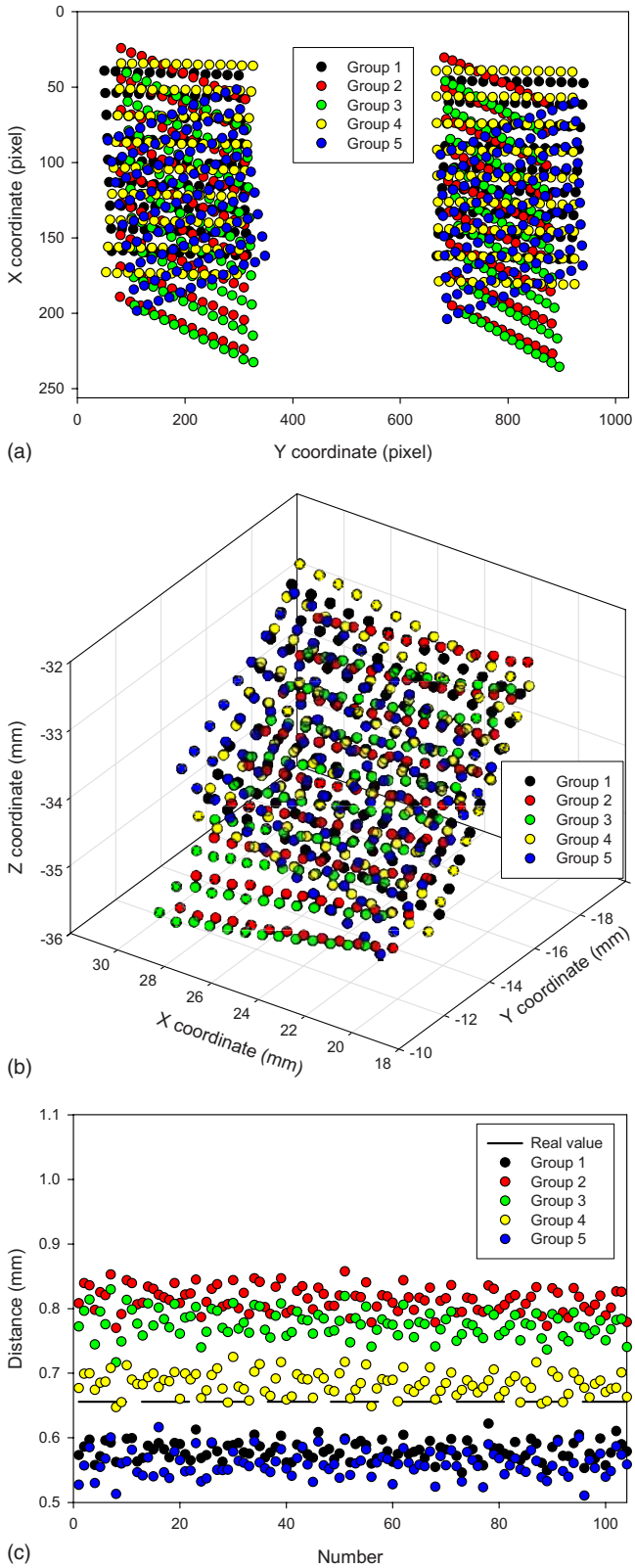

FIG. 5. (Color online) Error analysis for five different induced angles. (a) Extracted 2D coordinates in the left and right image coordinate systems. (b) Computed 3D coordinate in the world coordinate system. (c) Measured distances as a function of real distance for each mesh point.

B. Two and three dimensional velocity (Measured case)

Based on above calibration results, a laser spot welding case was measured by tracking one surface oxide particle movement. The particle displacements dependent on time are shown in Fig. 6(a), where the time step between successive image pairs is 1 millisecond. Five images show particle movement following an inward liquid flow pattern because of a positive surface tension gradient. The inward flow motion makes the weld pool surface concave.

Both 2D and 3D velocities are calculated as shown in Fig. 6(b). The 2D velocity is based on the distance of particle displacement projected on the sample surface. Based on the structure of the stereo adapter shown in Fig. 2, the coordinate values in the image Euclidean coordinate system for the left and right side views should be identical if and only if the object appears on the center line of the stereo adapter. However, particle movement does not follow such a line but moves on a 3D curved surface, which means the viewing angle for left and right views are not only different but also asymmetric. The relationship between image pixel and real distance in a 2D system are shown in Table I. The 2D velocity is computed from the 2D image Euclidean coordinate system for left and right side views; however, there is a difference between the 2D velocity values from left and right views, and both of them ignore the third component, which is normal to sample surface.

A schematic figure is shown in Fig. 6(c) in order to explain the relationship between 2D and 3D velocities. When a particle is moving on the weld pool surface, the 2D velocity is projected onto the surface as horizontal components from the 3D velocity; since the viewing angle is asymmetric these two components are not identical. Based on the 2D and 3D velocities shown in Fig. 6(b), the angle between the velocity components can be evaluated by simply dividing the 2D velocity by the 3D velocity as shown in Fig. 6(b). These are presented in Fig. 6(c) as angles α and β. It should be noted that the two 2D components are not perpendicular to each other. Figure 6(d) shows that when an object A is placed on the central line at the distance d in front of stereo adapter (zone I in Fig. 2), it is first reflected as A' by the outside longer mirror, and then as A'' by the shorter mirror. So A in front of stereo adapter is the same as A'' without the stereo adapter. Since there is a short distance D between the two mirrors, then the geometric relationship can be expressed as shown in Fig. 6(d), where the two mirrors are parallel to each other and the included angle between the mirror and lens is 45°. It is obvious that ω is less than 45°, and the viewing angle from the lens to A'' is $45°+\omega$. The angle ω is dependent on d and D viz: $\mathrm{arctg}(\omega)=1+2\sqrt{2}D/d$ and this condition is the same for both the left and right views. Thus, both of the viewing angles lie between 45°and 90°. As a result, the 2D velocity components are not exactly perpendicular to each other.

In Fig. 7, a cross section of the weld pool is polished to show the shape and the surface inclination after solidification. Measured angles are also shown in Fig. 7. The inward flow center is not stationary during welding, but oscillates around the geometric center of the weld pool, and the inclination angle of the weld pool surface during welding is variable and larger than the values measured after solidification of the weld pool. Although the solidified weld pool cannot be

Downloaded 15 Sep 2010 to 131.180.130.114. Redistribution subject to AIP license or copyright; see http://jap.aip.org/about/rights_and_permissions

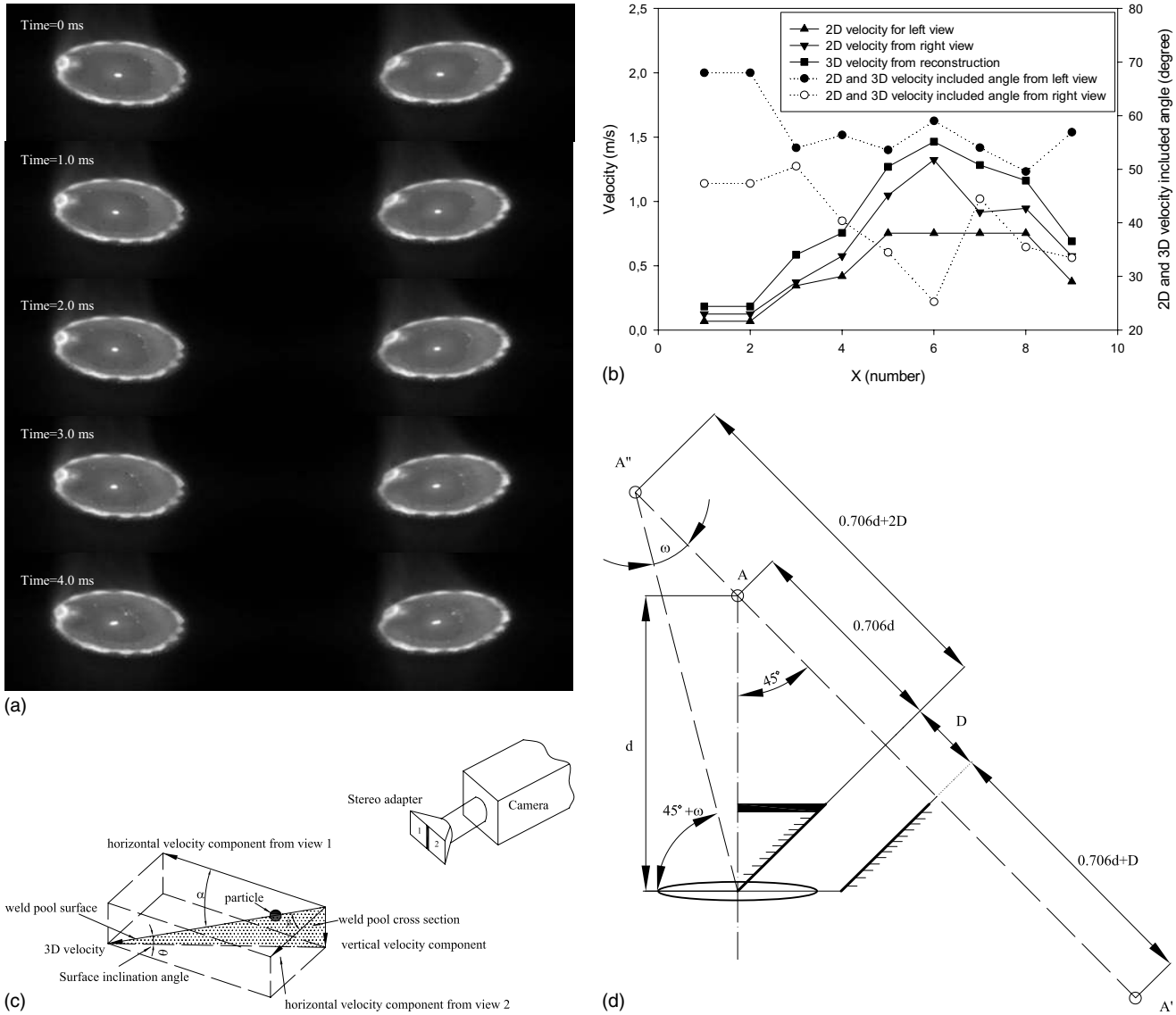

FIG. 6. Test case: Velocity from 2D and 3D measurements. (a) Particle flow motion. (b) 2D and 3D velocity based on the images shown in (a). (c) Relationship between 2D velocity and 3D velocity. (d) 2D viewing angle.

used to represent the weld pool shape during welding, it still gives a qualitative understanding of the inclination of the weld pool surface.

It is important to note that when the weld pool surface is not flat, not only is the flow motion complex, but it can also influence the heat and mass transfer. The inward flow can induce an interfacial phenomenon,[32,33] which has been shown to be unstable. When the inclination angle of the weld pool surface increases enough, weld pool surface collapse can result in the entrapment of a gas bubble, the result of such a collapse is visible in Fig. 7. The subsequent pool behavior should therefore be described as a two phase flow, since the flow velocity can be as high as 1 m/s in such a small channel. Here 3D measurement should provide more reliable information than simple 2D measurement.

TABLE I. 2D relationship between pixels and real distances.

Left view		Right view	
X (mm/pixel)	*Y* (mm/pixel)	*X* (mm/pixel)	*Y* (mm/pixel)
0.063 133	0.013 705	0.058 532	0.024 785

C. Weld pool surface inclination and accuracy analysis

As discussed above, different inclinations can lead to different assessments of accuracy since inclination moves some of the studied points out of the focal plane. For the 3D curved weld pool surface, the induced angle between the camera and particle flow direction is dependent on the camera inclination angle, the surface curvature, and the particle position. As is shown in Fig. 8, $\theta(0° < \theta < 90°)$ is the weld pool surface inclination angle to the horizontal plane, for a flat surface $\theta = 0°$. Theoretically, at the center of weld pool $\theta = 90°$ since the inward flow direction is vertically downward, but in real welding, this small interface area is a smooth curve since the surface tension is always there. The

Downloaded 15 Sep 2010 to 131.180.130.114. Redistribution subject to AIP license or copyright; see http://jap.aip.org/about/rights_and_permissions

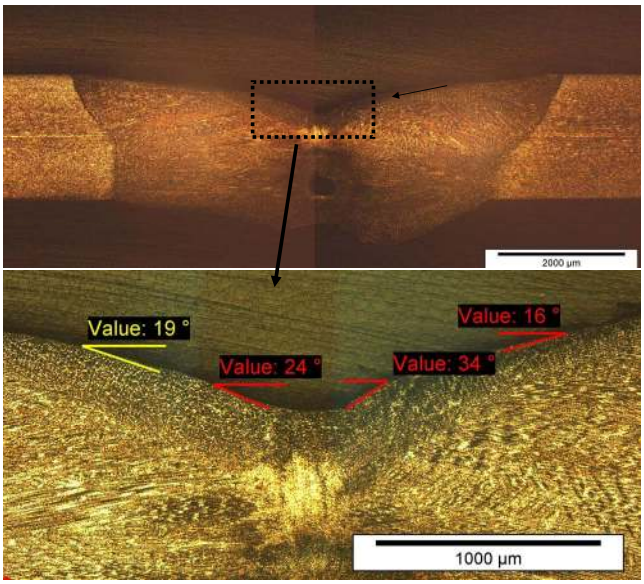

FIG. 7. (Color online) Cross section of the weld pool for a laser power of 2000 W and a welding duration of 2 s. The small black arrow shows the flow direction (top). Surface inclination angles in the center of the weld pool (bottom).

camera inclination angle to horizontal plane is γ. To observe the particles on the weld pool surface we must have $\gamma > \theta$ and due to experimental limitations $\gamma < 90°$.

Figures 8(b)–8(d) show three different representative positions on the weld pool surface labeled flow paths 1, 2, and 3 in Fig. 8(a), which meet at point O, the geometric center of weld pool surface. For the particle following flow path 1 [Fig. 8(b)], the induced angle between camera and weld pool surface is $\phi = \gamma - \theta$; a similar condition applies to flow path 3 where $\phi = \gamma + \theta$ [Fig. 8(d)]. Flow path 2 [Fig. 8(c)] lies perpendicular to the camera axis; the angle ϕ between the camera axis and the pool surface is therefore $\phi = \arccos[\sin(\gamma) \times \sin(\theta)]$. For the measurements made in this study, $0° < \theta < 35°$ and the camera inclination angle to the work piece surface $\gamma \approx 45°$. Thus the induced angles for flow path 1, 2, and 3, respectively range from $15° < \phi < 45°$, $66° < \phi < 90°$, and $45° < \phi < 75°$.

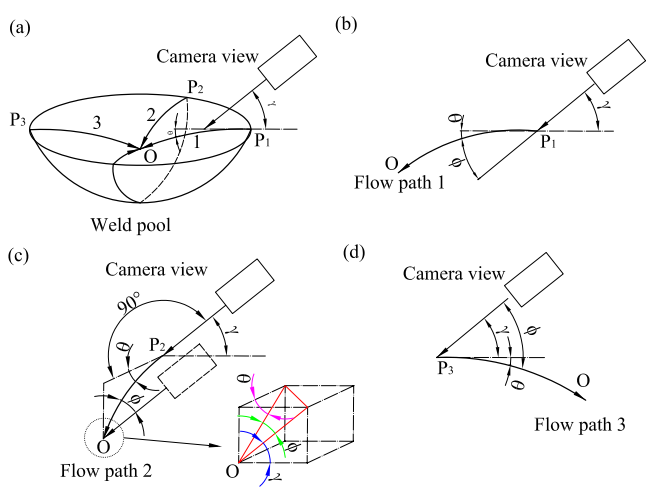

FIG. 8. (Color online) Induced angle between camera and inclination of weld pool surface.

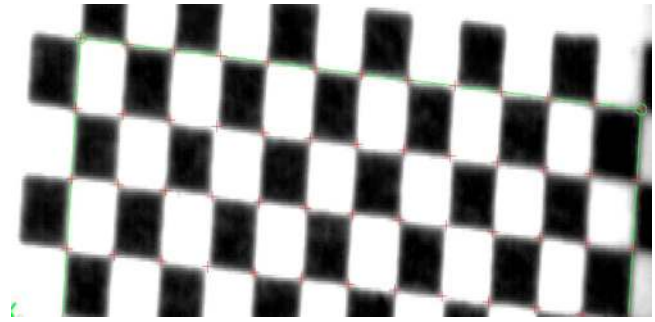

FIG. 9. (Color online) Enlarged calibration checkerboards.

The current 3D reconstruction results are based on particles lying on the weld pool surface between the positions of flow paths 2 and 3 [Fig. 8(a)]. This may be illustrated with reference to Fig. 6(a), where the movement of the white point on the top-right of the weld pool is followed. Only a very small region of the pool surface has an inclination angle $\theta > 30°$, as measured from the weld pool cross section in Fig. 7. For the velocity assessment, we chose particles located between the boundary and approximately 80% of the pool radius, since close to center of the weld pool, the flow motion is less stable and measurement errors increase. The induced angle ϕ between the camera and weld pool surface is the therefore larger than 45°. As already described in the calibration error analysis section, calibration group 1 had a camera to surface inclination of 45°, giving rise to a reconstruction error of 11.4%. In current measured case, the induced angle between particle flow direction and camera lens is larger than 45°. As a result, our current 3D reconstruction has a maximum error somewhat below this limit because of the higher average induce angle.

D. Error source

Calibration is the main factor influencing the measurement precision during 3D reconstruction. However, there are a number of other potential sources of error including the roughness of calibration board, spatial resolution of calibration checkerboard. The first is not thought to be significant in the present case as the board is flat to within a few microns. The spatial resolution of the checkerboard relates to the accuracy of printing and hence the accuracy to which the intersection points can be identified. Graininess in the image is illustrated in an enlarged section of the checkerboard shown in Fig. 9. For our purposes, a printing precision of 50 μm was employed. This is thought to give rise to the largest error since the square boundary is not sharp enough to distinguish the position of the corners with sufficient accuracy. Measurements of the distance between corner points resulted in an average error of ± 14 μm.

E. Potential application

This method can provide 3D point coordinates for a weld pool in a world coordinate system, if there are enough recognized points on the weld pool surface. It is then possible to obtain 3D surface profile measurements and flow velocity measurements for a weld pool under favorable cir-

Downloaded 15 Sep 2010 to 131.180.130.114. Redistribution subject to AIP license or copyright; see http://jap.aip.org/about/rights_and_permissions

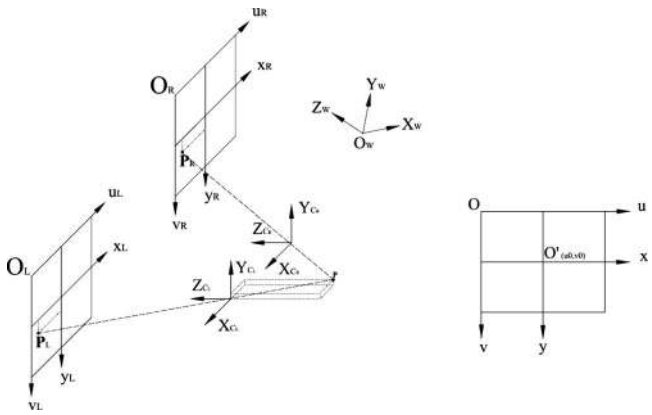

FIG. 10. Geometric relationships between the world coordinate system (w), camera coordinate system (c) and image coordinate system (Ref. 24).

cumstances. In well shielded welding conditions, the surface remains quite clean, without any oxide particles; adding an additional structured illumination laser, as used by Song and Zhang,[27,28] could offer an efficient way to reconstruct the weld pool surface and to track surface oscillations on both arc and laser generated weld pools. It is also possible to use this method when the object shape is a complex 3D component; however, the equipment arrangement is inherently more complex.

V. CONCLUSION

A novel method was used to study the fluid flow on the weld pool surface based on machine vision. By adding a simple stereo adapter to obtain two images on the same frame of a high speed camera, 3D coordinates in a world coordinate system are obtained. The qualitative flow motion and quantitative flow velocity are observed, and the method provides a novel way to study the liquid metal flow in the weld pool during welding.

VI. SUPPLEMENT

A video shows the particle flow motions during laser heating up the sample.[34]

ACKNOWLEDGMENTS

This research was carried out under Project No. MC8.05240 in the framework of the Research Program of the Materials Innovation Institute M2i (www.m2i.nl), the former Netherlands Institute for Metals Research.

APPENDIX: STEREO VISION ALGORITHM

1. Geometry relation between image and special coordinate system

In order to understand this stereo system mathematically, first, four coordinate systems[24] are introduced, which are shown in Fig. 10. They are the world Euclidean coordinate system with subscript w, the camera Euclidean coordinate system with subscript c, the image Euclidean coordinate system in 2D, uOv, and the image affine coordinate system $xO'y$. The image Euclidean and image affine coordinate systems, are in the same plane but have different origins. If point $O'(u_0,v_0)$ in the image Euclidean coordinate system is the origin of the image affine coordinate system, then the coordinate of any point of $P_i(u_i,v_i)$ in the image Euclidean coordinate system uOv can be expressed as

$$u_i = \frac{x_a}{dx} + u_0,$$

$$v_i = \frac{y_a}{dy} + v_0, \tag{A1}$$

where dx and dy are the physical scales of each pixel. Equation (A1) can be rewritten in matrix form as

$$\begin{bmatrix} u_i \\ v_i \\ 1 \end{bmatrix} = \begin{bmatrix} \frac{1}{dx} & 0 & u_0 \\ 0 & \frac{1}{dy} & v_0 \\ 0 & 0 & 1 \end{bmatrix} \begin{bmatrix} x_a \\ y_a \\ 1 \end{bmatrix}. \tag{A2}$$

A pinhole model is used to express the relationship between the image Euclidean coordinate system and the camera Euclidean coordinate system. As shown in Fig. 10, point $P_C(X_C,Y_C,Z_C)$ in the camera Euclidean coordinate system is projected onto the left image as point P_L and right image as point P_R. Assuming that f is the focal length, then Eq. (A3) can be used to express the projection relationship for point $P_C(X_C,Y_C,Z_C)$ in each camera Euclidean coordinate system and the image affine coordinate system, based on similar-triangles, where (x_a,y_a) is the coordinate in the image affine coordinate system,

$$\frac{f}{Z_c} = \frac{x_a}{X_c} = \frac{y_a}{Y_c}. \tag{A3}$$

which can be rewritten as

$$Z_c \begin{bmatrix} x_a \\ y_a \\ 1 \end{bmatrix} = \begin{bmatrix} f & 0 & 0 & 0 \\ 0 & f & 0 & 0 \\ 0 & 0 & 1 & 0 \end{bmatrix} \begin{bmatrix} X_c \\ Y_c \\ Z_c \\ 1 \end{bmatrix}. \tag{A4}$$

There is a unique relation between the world and each camera coordinate system given by the Euclidean transformation consisting of a translation $T(1\times 3)$ and rotation $R(3\times 3)$ matrix expressed by

$$\begin{bmatrix} X_C \\ Y_C \\ Z_C \end{bmatrix} = \begin{bmatrix} R & T \\ 0 & 1 \end{bmatrix} \begin{bmatrix} X_W \\ Y_W \\ Z_W \\ 1 \end{bmatrix}. \tag{A5}$$

Equations (A2), (A4), and (A5) represent all the relationships between the four coordinate systems, the relationship between the image coordinate system and the world Euclidean coordinate system can therefore be expressed as

Downloaded 15 Sep 2010 to 131.180.130.114. Redistribution subject to AIP license or copyright; see http://jap.aip.org/about/rights_and_permissions

$$Z_c\begin{bmatrix} u_i \\ v_i \\ 1 \end{bmatrix} = \begin{bmatrix} \alpha_x & 0 & u_0 & 0 \\ 0 & \alpha_y & v_0 & 0 \\ 0 & 0 & 1 & 0 \end{bmatrix}\begin{bmatrix} R & t \\ 0 & 1 \end{bmatrix}\begin{bmatrix} X_w \\ Y_w \\ Z_w \\ 1 \end{bmatrix} = M_1 M_2 P_w$$

$$= MP_w, \tag{A6}$$

where M is a 3×4 matrix, M_1 is a 3×4 intrinsic matrix, M_2 is a 4×4 extrinsic matrix. A calibration process will be introduced in the following steps to obtain the unknown parameters in matrix M.

2. Stereo point reconstruction

Both left and right side views can be processed using Eq. (A6) and are shown as follows:

$$Zc_1\begin{bmatrix} u_1 \\ v_1 \\ 1 \end{bmatrix} = \begin{bmatrix} m_{11}^1 & m_{12}^1 & m_{13}^1 & m_{14}^1 \\ m_{21}^1 & m_{22}^1 & m_{23}^1 & m_{24}^1 \\ m_{31}^1 & m_{32}^1 & m_{33}^1 & m_{34}^1 \end{bmatrix}\begin{bmatrix} X_w \\ Y_w \\ Z_w \\ 1 \end{bmatrix}, \tag{A7}$$

$$Zc_2\begin{bmatrix} u_2 \\ v_2 \\ 1 \end{bmatrix} = \begin{bmatrix} m_{11}^2 & m_{12}^2 & m_{13}^2 & m_{14}^2 \\ m_{21}^2 & m_{22}^2 & m_{23}^2 & m_{24}^2 \\ m_{31}^2 & m_{32}^2 & m_{33}^2 & m_{34}^2 \end{bmatrix}\begin{bmatrix} X_w \\ Y_w \\ Z_w \\ 1 \end{bmatrix}. \tag{A8}$$

Eliminating Zc_1 and Zc_2 yields

$$(u_1 m_{31}^1 - m_{11}^1)X + (u_1 m_{32}^1 - m_{12}^1)Y + (u_1 m_{33}^1 - m_{13}^1)Z = m_{14}^1 - u_1 m_{34}^1,$$

$$(v_1 m_{31}^1 - m_{21}^1)X + (v_1 m_{32}^1 - m_{22}^1)Y + (v_1 m_{33}^1 - m_{23}^1)Z = m_{24}^1 - v_1 m_{34}^1, (u_2 m_{31}^2 - m_{11}^2)X + (u_2 m_{32}^2 - m_{12}^2)Y + (u_2 m_{33}^2 - m_{13}^2)Z = m_{14}^2 - u_2 m_{34}^2, (v_2 m_{31}^2 - m_{21}^2)X + (v_2 m_{32}^2 - m_{22}^2)Y + (v_2 m_{33}^2 - m_{23}^2)Z = m_{24}^2 - v_2 m_{34}^2, \tag{A9}$$

where u_1, v_1 and u_2, v_2 can be obtained from the images, and X, Y, and Z represent the real 3D coordinates in world coordinate system. Calibration is required to determine $m_{i,j}^k (i=1,2,3;\ j=1,2,3,4;\ k=1,2)$. When these are known, a 3D coordinate in the world coordinate system can be computed for any pair of coordinate points (u_1,v_1), (u_2,v_2) from the image Euclidean coordinate system.

[1]G. Saeed and Y. M. Zhang, Meas. Sci. Technol. **18**, 2570 (2007).
[2]D. R. Atthey, J. Fluid Mech. **98**, 787 (1980).
[3]S. Kou and Y. H. Wang, Metall. Trans. A **17**, 2271 (1986).
[4]S. Kou and Y. H. Wang, Weld. J. (Miami, FL, U.S.) **65**, 63s (1986).
[5]S. Kou and Y. H. Wang, Metall. Trans. A **17**, 2265 (1986).
[6]H. G. Kraus, Weld. J. (Miami, FL, U.S.) **68**, 84s (1989).
[7]M. Tanaka, K.Waki, S.Tashiro, K.Nakata, E.Yamamoto, K.Yamazaki and K.Suauki, IIW Doc. 212–1122–08.
[8]M. Y. Krasnoperov, R. R. G. M. Pieters, and I. M. Richardson, Sci. Technol. Weld. Joining **9**, 501 (2004).
[9]J. Q. Gao and C. S. Wu, Sci. Technol. Weld. Joining **12**, 50 (2007).
[10]Z. Sun, Q. Chen, W. Zhang, Y. Chao, and P. Liu, Meas. Sci. Technol. **17**, 3212 (2006).
[11]J. J. Wang, T. Lin, and S. B. Chen, Int. J. Adv. Manuf. Technol. **26**, 219 (2005).
[12]Z. H. Yan, G. J. Zhang, H. M. Gao, and L. Wu, Sci. Technol. Weld. Joining **10**, 744 (2005).
[13]Y. H. Xiao and G. den Ouden, Weld. J. (Miami, FL, U.S.) **69**, 289 (1990).
[14]Y. H. Xiao and G. den Ouden, Weld. J. (Miami, FL, U.S.) **72**, 428 (1993).
[15]B. Y. B. Yudodibroto, M. J. M. Hermans, Y. Hirata, G. Den Quden, and I. M. Richardson, Sci. Technol. Weld. Joining **11**, 308 (2006).
[16]M. J. M. Hermans, B. Y. B. Yudodibroto, Y. Hirata, G. den Ouden, and I. M. Richardson, Mater. Sci. Forum **539–543**, 3877 2007.
[17]D. Delapp, G. Cook, A. Strauss and W. Hofmeister. Quantitative observations of surface flow and solidification on autogenous GTA weld pools, ASM proceedings of the international conference, trends in welding research, 2005.
[18]D. Delapp, Observations of Solidification and Surface Flow on Autogenous Tungsten Arc Weld Pools, Ph.D. thesis, Nashville, Tennessee, USA, 2005.
[19]P. Henrikson, *Mathematical Modelling of Weld Phenomena*, Vol. 7, Pp. 125–147, edited by H. Cerjak and H. K. D. H. Bhadeshia (Institute of Materials, London SW1Y 5DB, UK, 2005).
[20]P. Henrikson, Volvo Aero Corporation, U.S. Patent No. WO 03/086,695A, 2003.
[21]A. A. Matsunawa, M. Mizutani, and S. Katayama, Weld. Int. **17**, 431 2003.
[22]M. Mizutani, S. Katayama, and A. Matsunawa, Proc. SPIE **4831**, 208, 2003.
[23]C. X. Zhao, V. Steijn, I. M. Richardson, Z. Saldi, and C. R. Kleijn. Proceedings on the Eight International Conference on Trends in Welding Research, Pine Mountain, Georgia, USA, 1–6 June 2008 (unpublished).
[24]M. Sonka, V. Hlavac, and R. Boyle, *Image Processing, Analysis, and Machine Vision*, 3rd ed. (Thomson, Toronto, 2008).
[25]C. Mnich, F. Al-Bayat, C. Debrunner, J. Steele, and T. Vincent, ASME Proceedings, Japan-USA Symposium on Flexible Automation, Denver, CO, USA, 9–21 July 2004 (unpublished).
[26]D. B. Zhao, J. Q. Yi, S. B. Chen, L. Wu, and Q. Chen, ASME J. Manuf. Sci. Eng. **125**, 493 (2003).
[27]H. S. Song and Y. M. Zhang, Meas. Sci. Technol. **18**, 3751 (2007).
[28]H. S. Song and Y. M. Zhang, Weld. J. (Miami, FL, U.S.) **86**, 323 (2007).
[29]C. D. Yoo and J. Lee, 3D Measurement of Weld Pool Using Biprism Stereo Vision Sensor, http://joining1.kaist.ac.kr/research/vision.htm, Seoul National University.
[30]http://www.vision.caltech.edu/bouguetj/calib_doc/
[31]Z. Zhang, R. Deriche, O. Faugeras, and Q. T. Luong, Artif. Intell. **78**, 87 (1995).
[32]T. Zacharia, S. A. David, J. M. Vitek, and T. DebRoy. Metall. Trans. B **21**, 600–603 (1990).
[33]C. X. Zhao, V. van Steijn, I. M. Richardson, C. R. Kleijn, S. Kenjeres, and Z. Saldi, Sci. Technol. Weld. Joining **14**, 132 (2009).
[34]See EPAPS Document No. E-JAPIAU-105-158911. The current display speed is 100 frames/second. A 304 stainless steel sample was heated by a 3000W stationary Nd-Yag laser spot. Two weld pools are observed on the same frame. Inward flow motion induced by surface tension takes oxide particles moving from boundary to the center of the weld pool. For more information on EPAPS, see http:www.aip.org/pubservs/epaps.html.

Downloaded 15 Sep 2010 to 131.180.130.114. Redistribution subject to AIP license or copyright; see http://jap.aip.org/about/rights_and_permissions